Proceedings World Geothermal Congress 2026
Calgary, Canada, June 8 – 11, 2026

Petrographic Insights of an Ultramafic Analogue for CO_2 Storage and Geologic Hydrogen Production in Serpentinization-Driven Geothermal Systems

Jonathan Alexander[1]*, David McNamara[1]
Department of Earth, Ocean, and Ecological Sciences, University of Liverpool, United Kingdom[1]
jonathan.alexander@liverpool.ac.uk

Keywords: serpentinization, CO_2 mineralization, hydrogen generation, fluid–rock reaction, ultramafic, SEM, reservoir analogue

ABSTRACT

Serpentinized mafic and ultramafic lithologies offer dual potential as hosts for reactive CO_2 mineralization and as natural sources of hydrogen. This study presents petrographic and SEM microanalyses of serpentinized peridotite and orthopyroxenite from Connemara, western Ireland, assessing their relevance as analogues for serpentinization-driven geothermal systems. The Dawros Peridotite shows extensive fluid–rock interaction, recorded by serpentine, amphibole, talc, carbonate, magnetite, and chromite assemblages. Orthopyroxenite, composed of enstatite with minor clinopyroxene and chromite, is pervasively altered to talc, with fluid ingress promoting local magnetite formation and magnesite veining. Amphibole–serpentine–talc–carbonate assemblages indicate widespread serpentinization and natural CO_2 mineralization, producing magnesite and dolomite from reactive Mg^{2+}. Serpentinite brecciation and mesh textures suggest reaction-driven fracturing could have maintained permeability and supported fluid flow. Coexisting magnetite and carbonate veins reflect overlapping CO_2 sequestration and hydrogen-producing redox reactions. The generation of geological hydrogen is inferred to result primarily from Fe^{2+} oxidation during the formation of magnetite and serpentine from Fe-bearing enstatite (and olivine where present), while primary Fe-spinel may represent a contributory source. However, rates of H_2-generation (280–310 °C) and mineral carbonation (180–200 °C) peak at distinct temperature ranges, potentially limiting concurrent operation. Incomplete transformation toward magnesite–quartz (listvenite) assemblages indicates latent mineral carbonation potential. These findings highlight how Connemara's altered ultramafic rocks record natural processes of serpentinization and carbonation, offering insights into fluid–rock reactions relevant to CO_2 storage and resource studies.

1 INTRODUCTION

Anthropogenic CO_2 emissions are the primary driver of global climate change, necessitating multi-scale strategies for long-term carbon sequestration. In-situ mineral carbonation, where CO_2 reacts with divalent cation-bearing silicate minerals to form stable carbonates, is among the most secure and durable options. Ultramafic lithologies such as peridotite and serpentinite are of particular interest because of their high olivine content and corresponding MgO-rich chemistry. Peridotite, typically comprising 60–90% olivine, contains 40–50 wt% MgO ± CaO ± FeO, approximately double the reactive cation potential of basalts currently used for CO_2 injection in Iceland (Marini, 2006; Matter and Kelemen, 2009). These properties make ultramafic rocks among the most promising natural reservoirs for large-scale mineral carbonation.

Natural analogues, such as the 15,000 km^3 Samail Ophiolite in Oman, demonstrate the scale of potential ultramafic carbon storage, hosting extensive listvenites formed by complete carbonation of peridotite through sustained CO_2-fluid interaction (Paukert et al., 2012; Falk and Kelemen, 2015). Modeling suggests that adding just 1 wt% CO_2 to the Samail Ophiolite could sequester one-quarter of atmospheric carbon, suggesting that the cost and rate of carbonation are the limiting factors in developing this CO_2 storage resource (Matter and Kelemen, 2009; Streit et al., 2009).

To address rate limitations, geothermal mineral carbonation has been proposed to enhance in-situ CO_2 storage in ultramafic formations (Kelemen and Matter, 2008; Matter and Kelemen, 2009). In this approach, peridotite is hydraulically fractured and heated before CO_2-rich fluids are injected at elevated pressure. Exothermic heat from mineral carbonation and serpentinization sustains reservoir temperature and reactivity, promoting fracture formation. This strategy aims to reach and maintain optimal reservoir conditions (~185 °C, pCO_2 > 70 bar, pH ≈ 8) that can mineralize up to one tonne of CO_2 per cubic meter of rock annually (Kelemen et al., 2011). Offshore induced thermal convection is an alternative, slower method, using passive heating of subseafloor peridotite to circulate CO_2-bearing seawater through fractures (Kelemen and Matter, 2008; Kelemen et al., 2019).

Beyond carbon storage, ultramafic reservoirs are a potential geologic hydrogen source. Molecular hydrogen is released as a by-product of serpentinization through Fe^{2+} oxidation:

$$\underset{\text{Ferrous silicate}}{Fe^{2+}\text{-bearing silicate}} + \underset{\text{Water}}{H_2O} \rightarrow \underset{\text{Serpentine}}{(Mg,Fe)_3Si_2O_5(OH)_4} + \underset{\text{Magnetite}}{Fe_3O_4} + \underset{\text{Hydrogen}}{H_2} \quad (1)$$

However, mineral carbonation and serpentinization compete for dissolved Mg^{2+}, Fe^{2+}, and CO_2, and operate most efficiently at distinct temperature ranges: 185–200 °C for dissolution–carbonation, and 280–310 °C for serpentinization (Power et al., 2011; Miller et al., 2019). The relative rates and extent of these reactions are controlled by evolving permeability, fluid composition, and mineral-scale microstructures.

This study investigates the natural alteration of the Dawros peridotite in western Ireland using petrography and SEM–EDS mapping. The site exhibits diverse alteration assemblages and microtextures, enabling quantification of elemental redistribution and identification of reactive phases. By integrating microanalytical observations with broader geochemical frameworks, this work evaluates how natural alteration textures in peridotite could inform the kinetics of CO_2 mineralization and hydrogen generation.

2 MATERIALS AND METHODS

2.1 Geological Setting and Sampling

A series of partially layered and foliated mafic and ultramafic intrusions, collectively known as the Dawros–Currywongaun–Doughruagh Complex (DCDC) were syntectonically intruded at mid-crustal levels (~15 km) into Dalradian metasediments of northern Connemara, Ireland (Hunt et al., 2012). During cooling, they were metamorphosed to amphibolite facies, and subsequently serpentinized (Rothstein, 1957). The Dawros Peridotite (c. 475 Ma), the largest ultramafic intrusion of the DCDC, outcrops over ~1 km^2 onshore and may extend under Bunlahy Bay (Hunt et al., 2012). The ultramafic sequence comprises a lower harzburgite unit, interlayered with serpentinized dunite, and an upper lherzolite unit transitional from wehrlite, containing relict orthopyroxene and diopside (Rothstein, 1957). This succession is interpreted as basal cumulates of a partitioned magma chamber (Kanaris-Sotiriou and Angus, 1976). Microanalytical data were acquired from five samples of orthopyroxenite and serpentinite collected from outcrops at Dawros More (Figure 1). Two samples (D1, D2) were taken from outcropping orthopyroxenite, two further samples (D3, D4) were collected within the Harzburgite Group, and one samples (D5) from the Lherzolite Group (Hunt et al., 2012).

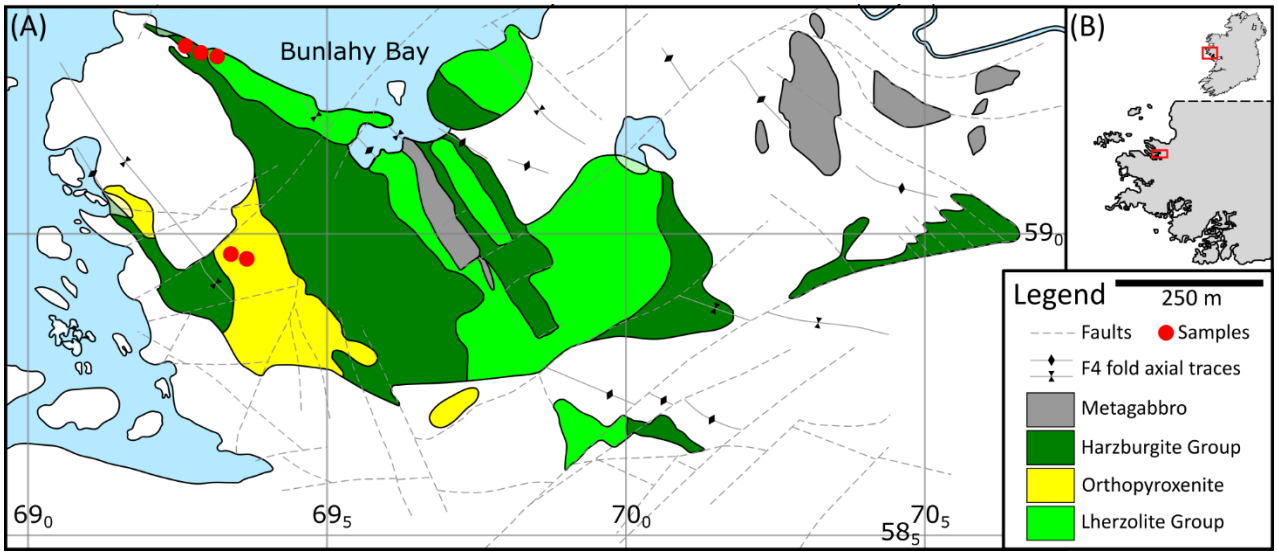


Figure 1: Maps of the sample locations. (A) Geological map of the Dawros Peridotite, taken from Hunt et al. (2012), marked with the five sample locations. (B) Inset maps of Ireland, and western Connemara.

2.2 Microanalytical Procedures

2.2.1 Petrography

Thin sections were analysed with transmitted light microscopy using a Leica DM750P microscope. Minerals were identified based on their optical properties, and the relative abundances of divalent cation-bearing minerals (e.g., olivine, pyroxene) were estimated. Mineral alteration and evidence of carbonate mineralization or serpentinization were also characterized.

2.2.2 Energy Dispersive X-ray Spectroscopy (EDS)

Thin sections were carbon coated (~50 nm) by thermal evaporation to minimize electrical charging. Backscattered electron (BSE) imaging was first used to identify regions of interest and highlight compositional variation. EDS analysis was performed using a Zeiss Gemini 450 FEG-SEM equipped with an Oxford Instruments X-Max20 silicon drift detector, at 15–20 kV accelerating voltage, ~1–10 nA beam current, 10 mm working distance, and 66 µs dwell time, using a 20 keV energy range across 2048 channels. EDS spectra and elemental maps were acquired and analyzed using AZtec software (v.6.1). Post-acquisition processing ("auto brightness" and "normalize brightness") enhanced contrast, exposing finer scale chemical variations, and allowed cross-comparison of elemental abundances. Point spectra were collected using the "Point & ID" function. Stoichiometric formulae were calculated by normalizing cations to a set oxygen basis. For complex minerals (e.g. amphiboles, serpentine) adjustments accounted for OH groups. For oxygen-free minerals, the anion count was set to one, and elemental ratios were used to suggest stoichiometry (e.g., pyrite, Fe:S = 1:2).

3 RESULTS

3.1 Petrography

D1 exhibits a crystalline adcumulate texture, dominantly comprising fractured, subhedral orthopyroxenes (~1 mm) (Figure 2A). Most display yellow-orange interference colors characteristic of bronzite, while some show second-order birefringence, suggesting Fe enrichment. In plain polarized light (PPL), crystals are largely colorless, with limited brown pleochroism. Rare interstitial areas with turquoise second-order birefringence likely correspond to anhedral, intergranular clinopyroxene. Two major veins contain an aphanitic carbonate fill (e.g., Figure 2A), with adjacent pyroxenes showing elevated birefringence and faint green pleochroism. Opaque minerals, likely magnetite, occur along vein margins and coat orthopyroxene surfaces. A smaller vein of opaque Fe-oxide, appears dark red in PPL. One corner of the sample is more altered, with crystals are replaced by talc.

D2 is more strongly altered (Figure 2B). Relict orthopyroxenes show elevated birefringence due to talc alteration and are deformed into lens-shaped masses within a talc matrix. Crystal fractures and surfaces are infiltrated by talc mosaics. Some acicular or elongated crystals may be amphibole after pyroxene. Minor opaque minerals are scattered in the talcose groundmass, while larger (~ 50 µm) equant opaques cluster adjacent to deformed orthopyroxene or amphibole (Figure 2B). Major fractures are coated with rust-colored Fe-oxide.

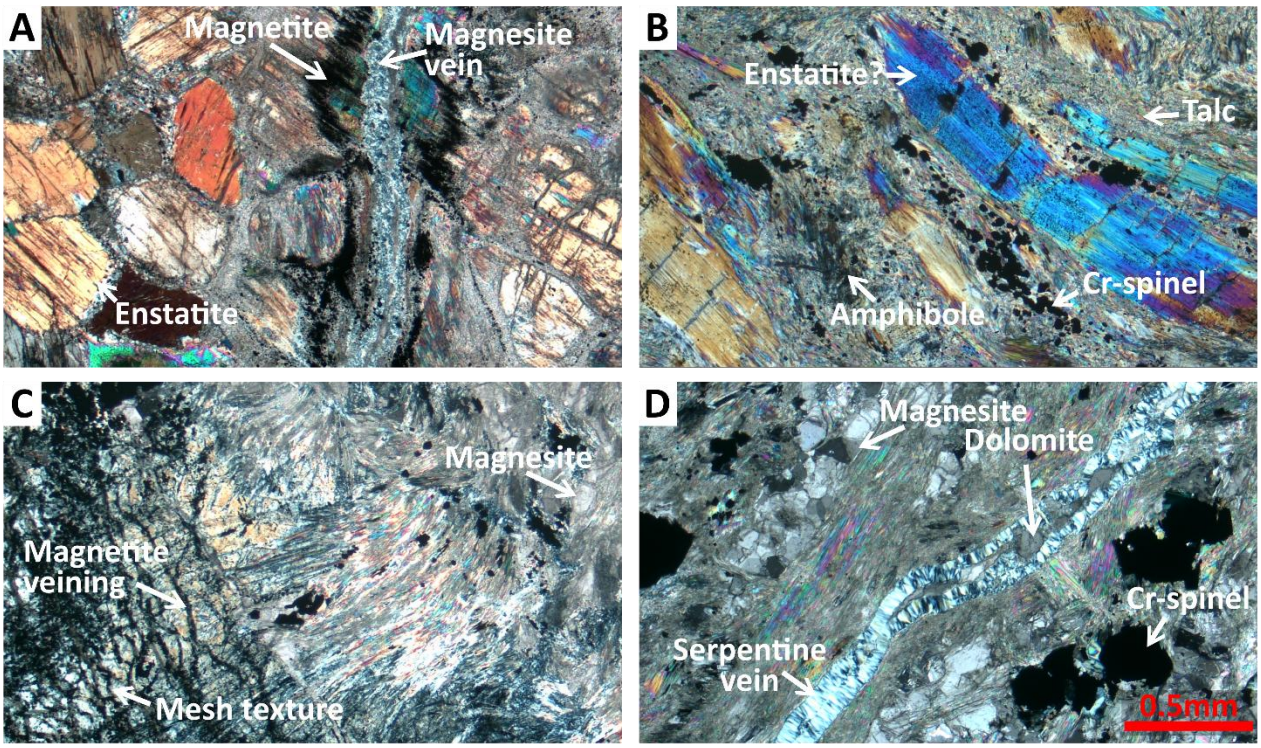


Figure 2: XPL photomicrographs. (A) Orthopyroxenite with carbonate vein and adjacent opaque minerals (D1). (B) Altered orthopyroxenite with strained, high birefringent, fractured crystals, with talcose rims (D2). (C) Feathered silicate assemblage in contact with serpentinite mesh texture (D3). (D) Talc-serpentine assemblage with serpentine-carbonate vein, carbonate aggregates and large chromite (D4).

D3 shows two distinct textural domains (Figure 2C). The majority of the thin section comprises a wavy, feather-like amphibole–talc–serpentine assemblage intergrown around equant, high-relief carbonate crystals. A second area features a darker mesh-textured fabric, heavily net-veined with opaque minerals, characteristic of serpentine mesh with magnetite (Figure 2C). Few relict mineral cores are present in the serpentine mesh, indicating nearly complete serpentinization. The serpentine groundmass is yellow in PPL and interfaces with the talcose area are marked by feather-like assemblages bent along vein structures. A thick (~0.5 mm) composite vein consists primarily of serpentine with two columns of twinned carbonate. Large (~0.5 mm) opaque masses are interpreted as Cr-spinel, with rims partially fragmented into irregular (~0.1 mm) masses.

D4 resembles D3 but lacks the mesh-textured serpentinite blocks. Acicular amphibole surrounds clusters of high-birefringent carbonate (Figure 2D). Small serpentine veins host central carbonate lenses, while a larger (0.5 mm) vein is fully carbonate-filled with growth banding. Large chromite masses (up to 0.7 mm) are more abundant than in D3, showing embayed, fragmented margins. Relict minerals are commonly pseudomorphed by acicular amphibole with aligned elongate opaques.

D5 is texturally homogenous, dominated by a serpentine mesh texture. Interconnected opaque minerals, interpreted as magnetite, outline former crystal boundaries from which feathered serpentine propagates. Mineral clusters within the mesh show high birefringence consistent with carbonate. Several veins (~0.2 mm thick) are similarly infilled with carbonate.

3.2 EDS

D1 orthopyroxene is chemically consistent with enstatite (Mg:Fe ≈ 1.8:0.2) with slightly higher Fe counts relative to the interstitial matrix. Small (~50 µm) clinopyroxene masses show high Ca EDS counts and lower Mg counts relative to the enstatite (Figure 3A), and are interpreted as augite (approx. $Mg_{1.2}Ca_{0.5}Fe_{0.1}Al_{0.1}$), with rare diopside also present. Carbonate veins show high Mg counts, lesser Fe, and minor Mn, indicating Fe-bearing magnesite ($MgCO_3$), while one small (~50 µm) carbonate phase with equal Ca and Mg suggests minor dolomite, $MgCa(CO_3)_2$. Enstatite adjacent to veins displays a minor decrease in Si counts, but other element abundances appear unchanged. Small (~20 µm) equant or lens-like Fe-oxide/oxyhydroxide (FeO/OH) phases, interpreted as magnetite, cluster around the magnesite veins. Smaller (~10 µm) Fe–Cr–Al oxides found across the whole area of acquisition, correspond to Al-bearing chromite, ($Fe^{2+}Al_{0.7}Cr_{1.3}O_4$).

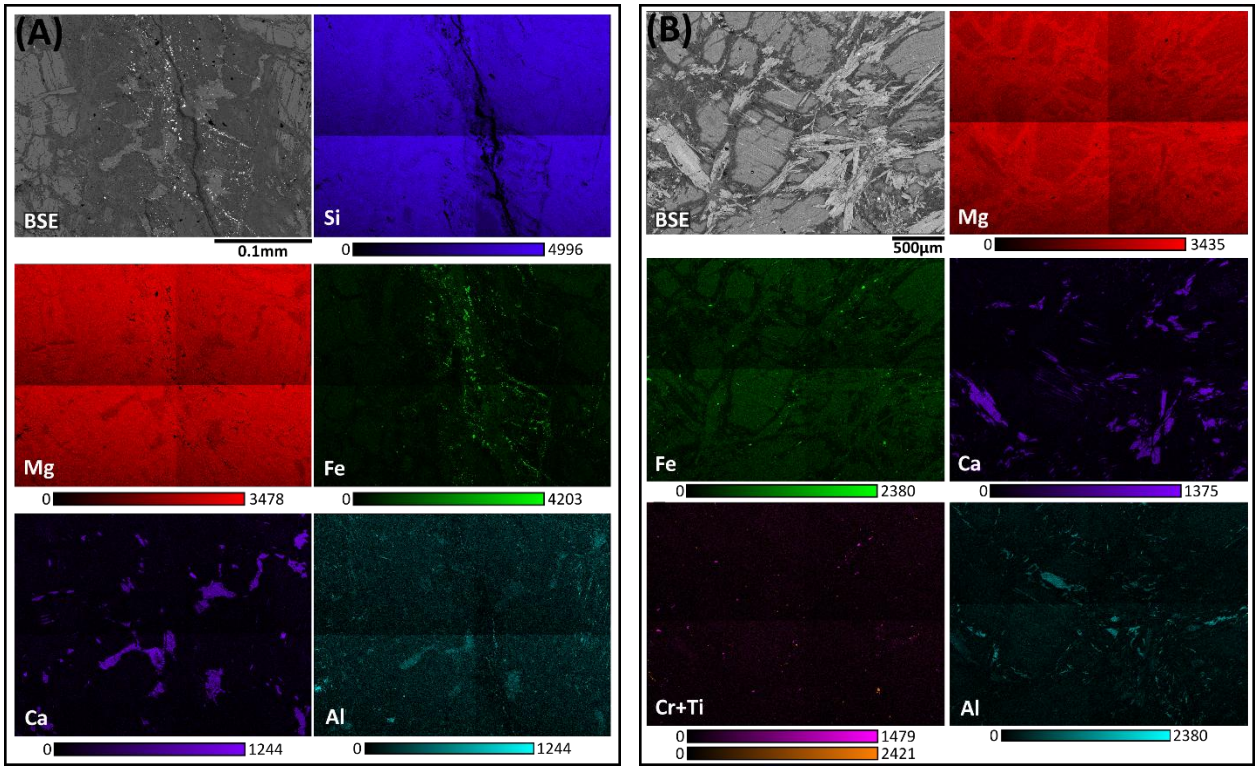


Figure 3: BSE and EDS of orthopyroxenite. (A) Magnesite vein (D1), Si, Mg, Fe, Ca, and Al element maps. (B) Talcose enstatite and acicular amphibole (D2), Mg, Fe, Ca, Cr, Ti, and Al, element maps.

D2 shows altered orthopyroxene with increased Fe, Si, and Al and decreased Mg EDS counts, suggesting partial transformation to Fe-bearing amphibole. Relict enstatite rims are altered to an intergranular phase with subtly lower Al and higher Fe and Mg counts (Figure 3B), consistent with Fe-bearing talc, $Fe_{0.2}Mg_{2.8}Si_4O_{10}(OH)_2$. Acicular crystals between talcose enstatite show compositional zoning, with rims corresponding to Fe-bearing amphibole ($FeMg_6Si_8O_{22}(OH)_2$) and cores potentially representing relict augite. Several enstatite crystals are fragmented parallel to mineral cleavage into smaller rafts within the talc matrix (Figure 2B). Large (~50 µm) Fe–Cr oxides of the Cr-spinel group, are more abundant in D2 than D1, and stoichiometric calculations yield approximately one Cr and two Fe cations, indicating Fe^{3+} enrichment and compositions consistent with ferrichromite ($Fe^{2+}(Cr,Fe^{3+})_2O_4$) or altered Al-bearing chromite (ferritchromit). Thin, elongate ilmenite shows high Ti counts with minor Mg and trace Mn, and is also more abundant in D2 than D1. Small (~10 µm) Ca-rich phosphate minerals within the talc closely match apatite, $Ca_{10}(PO_4)_6(OH,Cl)_2$.

D3 is mineralogically and chemically diverse. The groundmass shows high Mg, Si, O, and lesser Fe EDS counts, consistent with serpentine or talc. Several parallel veins comprise Fe-bearing magnesite. Magnesite is also commonly interspersed as clusters within the groundmass alongside smaller Ca-rich dolomite. Another vein displays high EDS counts of Mg, Si, O and Fe, and stoichiometric calculations indicate it is serpentine (Figure 4A). Clustered FeO/OH minerals adjacent to the vein are interpreted as magnetite. Relict mineral cores within the mesh-textured fabric are partially serpentinized, relict orthopyroxene. Some of these minerals have been pseudomorphed by dolomite adjacent to serpentine veining. A thick (>1 mm) composite vein consists of angular dolomite crystals, with a phase at the vein margin showing high Mg, Si, and O counts, indicative of serpentine. BSE imaging reveals zonation in the dolomite that is undetectable by EDS. Two large, conjoined FeO/OH minerals show distinct chemical zonation. The 0.1 mm-wide core has high EDS counts of Cr and lower Mn, Ti, and Co, with Al counts decreasing and Fe counts increasing towards a ~50 µm Fe-rich rim partially replaced by groundmass and magnesite. The core is identified as Al-bearing chromite ($Fe^{2+}Fe_{0.2}{}^{3+}Al_{0.7}Cr_{1.1}O_4$) with increasing Fe^{3+} substitution of Al^{3+} toward the rim. The spinel is enveloped by FeO/OH rims interpreted as magnetite, coinciding with elevated Al and minor Cr counts in the groundmass, possibly chlorite. Smaller (~10 µm) mineral phases across D3 and two larger (~25 µm) masses within a magnesite vein display Fe, Ni, and S counts consistent with pentlandite ($(FeNi)_9S_8$), while two additional ~25 µm Fe–Cu–S masses in the groundmass are identified as chalcopyrite.

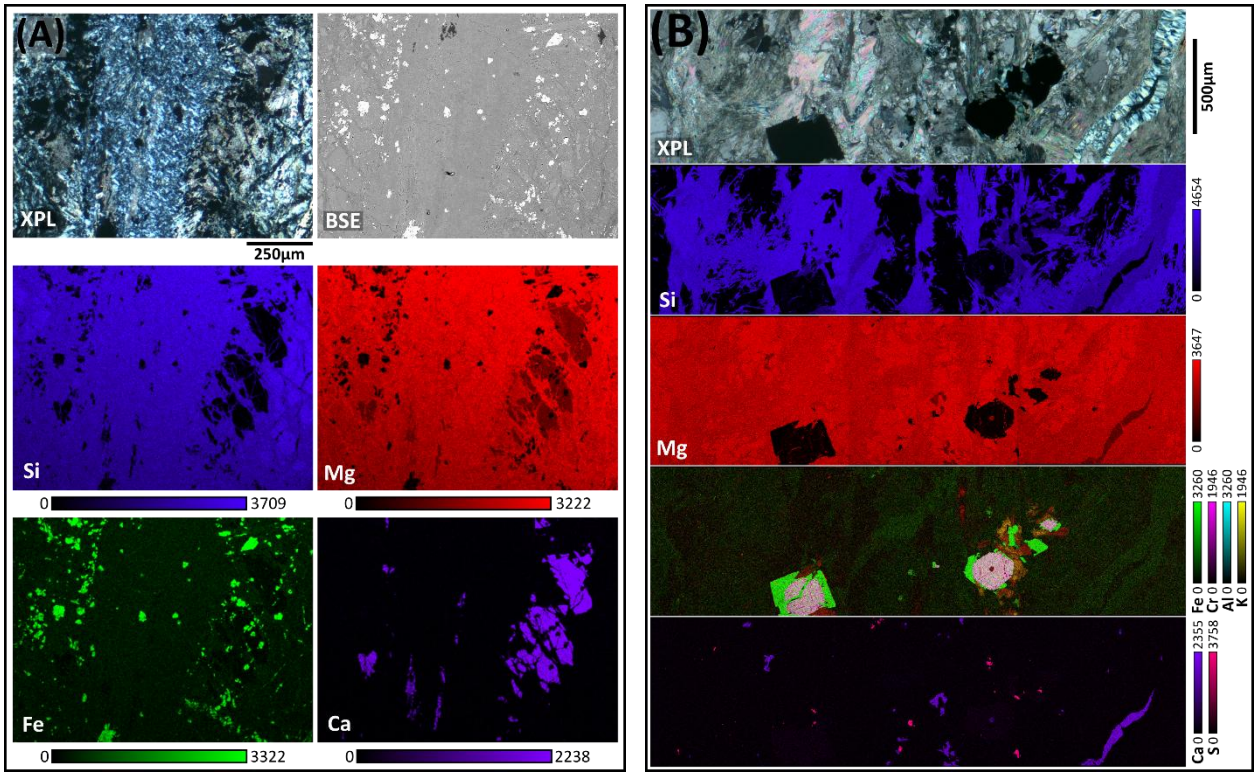


Figure 4: XPL, BSE, and EDS of serpentinized peridotite. (A) Serpentine veins, dolomite and magnetite (D3), Si, Mg, Fe, and Ca element maps. Dolomite partially infills mesh texture. (B) Amphibole-talc-carbonate groundmass, veining and chromite (D4), Si, Mg, Fe, Cr, Al, K, Ca, S element maps.

D4 is chemically similar to D3 but with greater variation in the groundmass and proportionally larger, zoned FeO/OH minerals (Figure 4B). The groundmass shows high EDS counts of Mg, Si, and O, with two phases distinguishable by birefringence and minor variations in Fe and Si counts. Areas lacking Fe counts correspond to a highly birefringent phase identified as talc, that is surrounded by Fe-bearing acicular assemblages identified as amphibole (~$Fe_{0.4}Mg_{6.6}Si_8O_{22}(OH)_2$), though they may also represent serpentine. Both phases are interspersed with large areas of magnesite and minor dolomite. Veining is variable, with a prominent (~0.5 mm) branched vein of dolomite and, more commonly, thinner (~0.2 mm) serpentine veins hosting either magnesite clusters or (≤50 µm) dolomite lenses ≤50 µm (Figure 4B). Large subhedral oxides are sharply zoned, with Al-rich spinel cores (~$Mg_{0.3}Fe_{0.7}^{2+}Fe_{0.2}^{3+}Cr_{0.9}Al_{1.1}O_4$) and ferrichromit rims showing higher Fe, minor Ti, and lower Al counts. Cr and Mn counts remain uniform across the oxides. The spinel is surrounded by a partially broken rim of Fe-oxide, interpreted petrographically as magnetite. In some areas (Figure 4B), the spinel is entirely ferritchromit with thicker rims of magnetite. Accessory minerals include minor (~10 µm) ilmenite (high Ti, Fe) and sulfides of pentlandite (Fe, Ni, S) and pyrite (Fe, S), with larger (~50 µm) opaque grains showing S–Ni–Fe zonation indicative of composite pentlandite–pyrite.

EDS analysis of D5 shows a homogeneous groundmass dominated by serpentine forming a mesh texture, interlinked with dolomite, with EDS counts indicating slightly higher Ca than Mg, and magnetite outlining former crystal boundaries (Figure 5). Carbonate and magnetite are spatially associated within the mesh. Cr-spinel is absent, while accessory pentlandite occurs as small (~5 µm) inclusions embedded within magnetite. Relict, primary silicate phases are minimal.

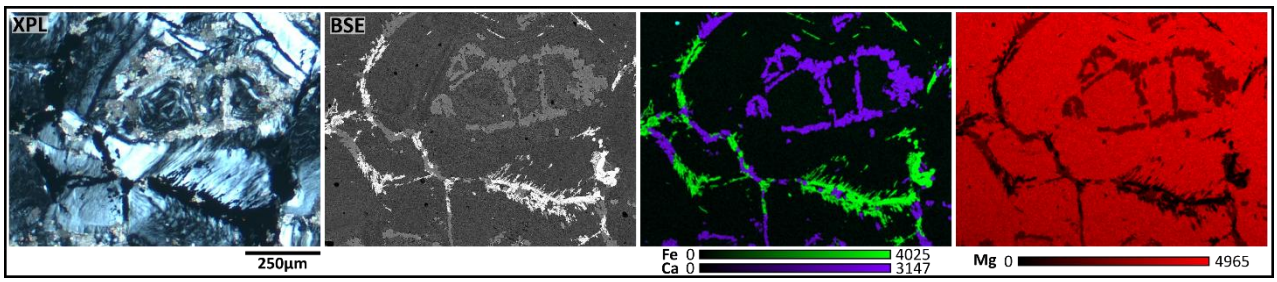


Figure 5: XPL, BSE, and EDS element mapping (Fe, Ca, Mg) for D5. Homogenous serpentine ($Mg_{2.9}Fe_{0.1}Si_2O_7$) mesh texture with Ca-rich dolomite and Fe-oxide (magnetite), lacking chromite.

4 DISCUSSION

4.1 Orthopyroxenite (D1–D2)

EDS mapping data determined that orthopyroxenite mostly comprises Fe-bearing enstatite, possibly of bronzite variety with high birefringence resulting from minor Fe content, impacting refractive indices. The high Mg orthopyroxenite suggests mineral carbonation will predominantly store CO_2 as magnesite. Dissolution of enstatite proceeds via the liberation of Mg from its crystal structure asynchronous with Si, creating leached layers on the surfaces of dissolved enstatite (Oelkers, 1999; Oelkers and Schott, 2001). Si-bonds are not rearranged through the replacement of Mg via hydrolysis, leaving the enstatite structure partially intact during Mg liberation (Oelkers, 1999). Because silica polymerization is higher in pyroxene than in olivine, complete dissolution will occur at a slower rate (Power et al., 2013). Thus, although both are suitable due to their cation abundance, peridotite composed solely of pyroxene, such as D1, will exhibit a slower dissolution rate compared to those containing olivine. However, an elevated Fe content may enhance the dissolution of Fe-bearing enstatite through iron oxidation (Hoch et al., 1996). Furthermore, exsolution lamellae, parallel to the (100) axis, are noted within the enstatite at Dawros. Lamellae nucleate within imperfections in the crystal and might cause structural defects that aid the dissolution of enstatite (Scherer, 1999). Microscale permeability may locally increase if fluids accessed crystal fractures, drastically increasing reactive surface area for mineral carbonation.

Two magnesite veins in D1 exemplify the natural carbonation of Dawros orthopyroxenite. Magnesite veining indicates some liberated Mg^{2+} (possibly from orthopyroxene dissolution) has already been consumed by mineral carbonation. Pervasive alteration of orthopyroxene (e.g. D2) to serpentine, talc, and magnetite, indicates further serpentinization and carbonation has progressed. This is impactful on carbonation rates as the development of serpentine and talc on the mineral surfaces passivates them, inhibiting further orthopyroxene dissolution, and causing these altered minerals to act as the initial reactant instead. Meanwhile, several FeO/OH phases are observed adjacent to magnesite veining (D1), suggesting Fe oxidation occurs during dissolution and subsequent mineral carbonation. Whilst EDS cannot discern between Fe^{2+} and Fe^{3+}, these FeO/OH phases are interpreted as magnetite, a common secondary Fe-oxide formed during alteration. This indicates that Fe^{2+}, liberated from dissolution of Fe-bearing phases such as olivine, augite, or Fe-bearing enstatite, has oxidized, potentially

releasing molecular hydrogen as a byproduct along fractures and fluid pathways. Fe^{2+} oxidation may also have occurred during serpentine alteration, although this cannot be confirmed by EDS as the Fe^{2+}/Fe^{3+} ratio is unknown.

4.2 Talc–Serpentine–Carbonate Lithologies (D3–D5)

Primary mineralogy of D3–D5 is undiscernible due to extensive alteration though is suggested to be harzburgite or lherzolite (Hunt et al., 2012). Unaltered, these lithologies would have high dissolution rates given their olivine content, which is perhaps what resulted in their pervasive alteration to amphibole, serpentine, talc, magnesite, and dolomite. Sampling locations of D3–5 were relatively contiguous, suggesting that serpentinization and talc-carbonate alteration is laterally variable. D3–5 show extensive natural mineral carbonation, suggesting a high potential for CO_2 storage. Magnesite, the dominant groundmass carbonate, will have formed from the carbonation of orthopyroxene (mainly enstatite), olivine, clinopyroxene, talc, or serpentine. Dolomite veining will have precipitated from fluids richer in Ca^{2+}, possibly from clinopyroxene dissolution. Dolomite often occurs within serpentine veins, indicating local precipitation after serpentine. It may represent the earliest precipitated carbonate because of a limited abundance of Ca-bearing minerals, or the latest precipitated carbonate from the infiltration of Ca-rich fluids (Bjerga et al., 2015).

Serpentinization progresses under largely isochemical conditions through peridotite hydration, propagating from olivine/pyroxene boundaries and gradually enclosing crystal core with aggregates of lizardite, chrysotile, and polygonal serpentine (Coleman and Keith, 1971; Viti and Mellini, 1998). As serpentine minerals occupy a larger volume than the primary anhydrous minerals they replace, the rock expands. Where the volume increase cannot be accommodated, cracking occurs, extending into fresh peridotite and facilitating further serpentinization (O'Hanley, 1992; Kelemen and Hirth, 2012). Crystal boundaries act as weaknesses during stress-induced fracturing, creating fluid pathways for carbonation or serpentinization (Shimizu and Okamoto, 2016). This mechanism is interpreted to have formed the serpentine mesh texture displayed in D5 and in regions of D3. Magnetite or carbonate has precipitated within these veins through oxidation and carbonation, respectively, underpinning geological hydrogen formation and CO_2-mineralization. However, the two mesh textures observed in the Dawros Peridotite (D3 and D5) vary as carbonate is only observed in mesh veins within D5, possibly because circulating fluids were rich enough in CO_2 or at optimal conditions (e.g. temperature, pH) to stabilize such phases.

Dissolution studies observe that Mg-leaching in serpentine veins produces a porous siliceous residue, opening pathways for further dissolution, and reaction-induced cracking promotes faster dissolution in serpentinite than in pyroxene-rich harzburgite (Lacinska et al., 2017). Serpentine minerals can store similar, or slightly greater, quantities of CO_2 than pyroxene of the same mass, although olivine is the most effective (Power et al., 2013). Therefore, depending on the primary composition of the peridotite, serpentinization may have a positive or negative impact on the tonnage of CO_2 able to be stored, provided carbonation has not already occurred.

Whilst modest natural carbonation coexists with serpentinization, extensive carbonate mineralization typically represents a separate hydrothermal event (Power et al., 2013). This is exemplified in D3 and D4, which display extensive talc and carbonate mineralization. Talc assemblages represent the secondary alteration of the silicates within these rocks to serpentine, tremolite, chlorite, as well as Mg-rich carbonates (Abdel-Rahman et al., 2022). Minor variations in the compositions of talc, carbonate and serpentine minerals will result from local variations in the proportion of pyroxene to olivine in the original groundmass. The alteration of the Dawros Peridotite to talc–carbonate assemblages is interpreted to be a product of shearing, evident from the deformation of relict minerals, and the circulation of CO_2-rich and H_2O-rich fluids derived from amphibolite-grade metamorphism. The stability of a talc–carbonate assemblage is confined to temperatures < 550 °C and $X_{CO2} \geq 0.02$ based on thermodynamic modeling studies (Bjerga et al., 2015). It could be assumed that serpentine and brucite are the primary minerals altering to talc, although evidence suggests that the orthopyroxenite (D2) was not completely serpentinized before talc formation, as relics are still discernible. The incomplete serpentinization before talc formation contrasts with findings from various experimental and field studies, which typically indicate complete serpentinization prior to talc formation, although this can occur for orthopyroxenite lacking olivine and brucite (Hansen et al., 2005; Bjerga et al., 2015).

Despite natural mineral carbonation of serpentinized lithologies (e.g. Dawros), a considerable abundance of Mg^{2+} still comprises the framework of serpentine and talc. Complete alteration to talc–carbonate assemblages represents approximately half of the carbonation potential for serpentinite, and further carbonation is required before the formation of magnesite–quartz assemblages characterizing fully carbonated peridotite, known as listvenite (Hansen et al., 2005; Kelemen et al., 2011). Therefore, there is still potential for CO_2 mineralization in the altered serpentinite of the Dawros Peridotite via talc and the remaining serpentine. Dissolution rates for talc

at acidic pH are possibly similar to enstatite due to comparable mechanisms of decomposition (Saldi et al., 2007; Power et al., 2013). The fractured and brecciated appearance of the reservoir suggests good permeability for in-situ mineral carbonation. Otherwise, the low hardness of talc might make it cheap to excavate as a source of Mg^{2+} for surficial mineralization pilots.

Accessory minerals include pentlandite, often intergrown with magnetite, and very rare ilmenite. Major oxide minerals are zoned Cr-spinel present in both altered orthopyroxenite (D2) and talc-carbonate-serpentinite (D3 and D4). Chemical zonation in Cr-spinel shows abrupt transitions from an Al-rich cores to a ferritchromit rims. Spinel was initially Al-rich but underwent a two-stage alteration: first, substitution of Al^{3+} by Fe^{3+} and minor replacement of Mg^{2+} by Fe^{2+} formed ferritchromit, typical of amphibolite-grade metamorphism (Saumur and Hattori, 2013); second, magnetite reaction rims formed, consistent with other studies (Merlini et al., 2009; Saumur and Hattori, 2013). Polygonal, crosscutting fractures in large Cr-spinel grains, often filled with serpentine or talc, indicate trellis exsolution or octahedral partings (Saumur and Hattori, 2013). Surrounding Al-rich zones are interpreted as clinochlore derived from Al^{3+}, liberated during ferritchromit alteration and reacting with serpentine and H_2O (Saumur and Hattori, 2013). During mineral carbonation, minor Mg^{2+} liberated during ferritchromit and magnetite alteration could contribute to Mg-carbonate formation, while Fe^{2+} in solution is oxidized, potentially generating geological H_2. At later stages of mineral carbonation, magnetite may progressively alter, leaching Fe^{2+}, and incorporating it into Fe-bearing magnesite until the formation of listvenite (Hansen et al., 2005). Although these FeO/OH reactions contribute to carbonation only in a minor capacity, they may impact local H_2 production and redox evolution.

4.3 Feasibility of Hydrogen Production with Mineral Carbonation

Hydrogen generation during serpentinization is closely linked to both rock composition and fluid-rock interactions, and these processes can intersect with mineral carbonation in ultramafic reservoirs (Klein et al., 2021; McCollom and Bach, 2009). Olivine-rich lithologies typically produce more H_2 than pyroxene-dominated rocks, but modeling suggests that dunite, harzburgite, and lherzolite can generate similar H_2 yields under the same temperature conditions (Klein et al., 2013). At Dawros, the coexistence of partially altered orthopyroxenite and serpentinite indicates that mineralogy locally controls hydrogen production, with Fe^{2+} oxidation occurring in magnetite veins and mesh textures. Temperature and pressure are critical controls, with H_2 generation increasing at intermediate temperatures (200–400 °C) and higher pressures, reaching up to ~244 mmol/kg at 315 °C in olivine-rich systems (McCollom and Bach, 2009; Klein et al., 2021; Rezaee, 2025), yet acidic CO_2-rich fluids can suppress H_2 production by shifting Fe^{2+} oxidation pathways and promoting carbonate formation, thereby limiting the amount of hydrogen released during serpentinization (Godard et al., 2013; McCollom et al., 2020; Luhmann et al., 2017). While thermodynamic predictions suggest that H_2 could react with CO_2 to form methane via Sabatier reactions, experimental studies indicate methane formation is kinetically limited under natural and injection conditions (<0.04% conversion; McCollom and Seewald, 2001). Reaction-induced cracking, evident in serpentine mesh textures, enhances permeability and reactive surface area, sustaining both hydrogen release and CO_2 mineralization. Overall, the Dawros peridotite demonstrates how mineralogy, microstructural evolution, and fluid chemistry collectively influence hydrogen production and its interplay with ongoing carbonation, highlighting the dual potential of ultramafic reservoirs as CO_2 sinks and geological hydrogen sources.

5 CONCLUSION

- Orthopyroxenite of the Dawros Peridotite, composed of enstatite, minor clinopyroxene and chromite, is pervasively altered to talc, with fluid ingress driving local magnetite formation and magnesite veining.
- Amphibole–serpentine–talc–carbonate assemblages record extensive serpentinization and natural CO_2 mineralization, producing magnesite and dolomite from reactive Mg^{2+}.
- Serpentinite textures (brecciation, mesh veining) suggest reaction-driven fracturing could have maintained permeability, sustaining fluid flow and carbonation.
- Coexisting magnetite and carbonate veins reflect overlapping CO_2 sequestration and hydrogen-producing redox reactions within the same system.
- Geological hydrogen will have primarily derived from Fe^{2+} oxidation (forming magnetite and serpentine) of Fe-bearing enstatite (and olivine where present), while spinel may represent a minor source.
- However, serpentinization-derived H_2 generation (280–310 °C) and mineral carbonation (180–200 °C) rates occur in distinct temperature regimes, suggesting limited concurrent efficiency of both processes.
- Incomplete transformation to magnesite–quartz (listvenite) assemblages demonstrates that significant Mg^{2+} remains bound within silicate minerals, indicating residual mineral carbonation capacity.

Acknowledgements

These results form part of a MS project funded by the Sustainable Energy Authority of Ireland. Fieldwork assistance from Dr. John Conneally. SEM-EDS acquisition undertaken at University of Liverpool SEM Shared Research Facility, supported and assisted by Dr. Joe Gardner.

REFERENCES

Abdel-Rahman, A.M., El-Desoky, H.M., Shalaby, B.N.A., Awad, H.A., Ene, A., Heikal, M.A., El-Awny, H., Fahmy, W., Taalab, S.A., and Zakaly, H.M.H.: Ultramafic Rocks and Their Alteration Products From Northwestern Allaqi Province, Southeastern Desert, Egypt: Petrology, Mineralogy, and Geochemistry, *Frontiers in Earth Science*, **10**, (2022).

Bjerga, A., Konopásek, J., and Pedersen, R.B.: Talc–carbonate alteration of ultramafic rocks within the Leka Ophiolite Complex, Central Norway, *Lithos*, **227**, (2015), 21–36.

Coleman, R.G., and Keith, T.E.: A Chemical Study of Serpentinization—Burro Mountain, California, *Journal of Petrology*, **12**, (1971), 311–328.

Falk, E.S., and Kelemen, P.B.: Geochemistry and petrology of listvenite in the Samail ophiolite, Sultanate of Oman: Complete carbonation of peridotite during ophiolite emplacement, *Geochimica et Cosmochimica Acta*, **160**, (2015), 70–90.

Hoch, A.R., Reddy, M.M., and Drever, J.I.: The effect of iron content and dissolved O_2 on dissolution rates of clinopyroxene at pH 5.8 and 25°C: preliminary results, *Chemical Geology*, **132**, (1996), 151–156.

Hunt, E., O'Driscoll, B., and Daly, J.S.: Parental magma composition of the syntectonic Dawros Peridotite chromitites, NW Connemara, Ireland, *Geological Magazine*, **149**, (2012), 590–605.

Kanaris-Sotiriou, R., and Angus, N.S.: The Currywongaun-Doughruagh syntectonic intrusion, Connemara, Ireland, *Journal of the Geological Society*, **132**, (1976), 485–508.

Kelemen, P., Benson, S.M., Pilorgé, H., Psarras, P., and Wilcox, J.: An Overview of the Status and Challenges of CO_2 Storage in Minerals and Geological Formations, *Frontiers in Climate*, **1**, (2019).

Kelemen, P.B., and Hirth, G.: Reaction-driven cracking during retrograde metamorphism: Olivine hydration and carbonation, *Earth and Planetary Science Letters*, **345–348**, (2012), 81–89.

Kelemen, P.B., and Matter, J.: In situ carbonation of peridotite for CO_2 storage, *Proceedings of the National Academy of Sciences*, **105**, (2008), 17295–17300.

Kelemen, P.B., Matter, J., Streit, E.E., Rudge, J.F., Curry, W.B., and Blusztajn, J.: Rates and Mechanisms of Mineral Carbonation in Peridotite: Natural Processes and Recipes for Enhanced, in situ CO_2 Capture and Storage, *Annual Review of Earth and Planetary Sciences*, **39**, (2011), 545–576.

Klein, F., Bach, W., and McCollom, T.M.: Compositional controls on hydrogen generation during serpentinization of ultramafic rocks, *Lithos*, **178**, (2013), 55–69.

Lacinska, A.M., Styles, M.T., Bateman, K., Hall, M., and Brown, P.D.: An Experimental Study of the Carbonation of Serpentinite and Partially Serpentinised Peridotites, *Frontiers in Earth Science*, **5**, (2017).

Marini, L.: Geological Sequestration of Carbon Dioxide: Thermodynamics, Kinetics, and Reaction Path Modeling, *Elsevier*, (2006).

Matter, J.M., and Kelemen, P.B.: Permanent storage of carbon dioxide in geological reservoirs by mineral carbonation, *Nature Geoscience*, **2**, (2009), 837–841.

McCollom, T.M., and Bach, W.: Thermodynamic constraints on hydrogen generation during serpentinization of ultramafic rocks, *Geochimica et Cosmochimica Acta*, **73**, (2009), 856–875.

McCollom, T.M., Klein, F., Solheid, P., and Moskowitz, B.: The effect of pH on rates of reaction and hydrogen generation during serpentinization, *Philosophical Transactions of the Royal Society A: Mathematical, Physical and Engineering Sciences*, **378**, (2020), 20180428.

McCollom, T.M., and Seewald, J.S.: A reassessment of the potential for reduction of dissolved CO_2 to hydrocarbons during serpentinization of olivine, *Geochimica et Cosmochimica Acta*, **65**, (2001), 3769–3778.

Miller, Q.R.S., Schaef, H.T., Kaszuba, J.P., Gadikota, G., McGrail, B.P., and Rosso, K.M.: Quantitative Review of Olivine Carbonation Kinetics: Reactivity Trends, Mechanistic Insights, and Research Frontiers, *Environmental Science & Technology Letters*, **6**, (2019), 431–442.

Oelkers, E.H.: A Comparison of Forsterite and Enstatite Dissolution Rates and Mechanisms, in Jamtveit, B. and Meakin, P. eds., Growth, Dissolution and Pattern Formation in Geosystems, *Springer Netherlands*, (1999), 253–267.

Oelkers, E.H., and Schott, J.: An experimental study of enstatite dissolution rates as a function of pH, temperature, and aqueous Mg and Si concentration, and the mechanism of pyroxene/pyroxenoid dissolution, *Geochimica et Cosmochimica Acta*, **65**, (2001), 1219–1231.

O'Hanley, D.S.: Solution to the volume problem in serpentinization, *Geology*, **20**, (1992), 705–708.

Paukert, A.N., Matter, J.M., Kelemen, P.B., Shock, E.L., and Havig, J.R.: Reaction path modeling of enhanced in situ CO_2 mineralization for carbon sequestration in the peridotite of the Samail Ophiolite, Sultanate of Oman, *Chemical Geology*, **330–331**, (2012), 86–100.

Power, I.M., Wilson, S.A., Thom, J.R., Dipple, G.M., and McCollom, T.M.: Carbon Mineralization: From Natural Analogues to Engineered Systems, *Reviews in Mineralogy and Geochemistry*, **77**, (2013), 305–360.

Rezaee, R.: Quantifying Natural Hydrogen Generation Rates and Volumetric Potential in Onshore Serpentinization, *Geosciences*, **15**, (2025), 112.

Rothstein, A.T.V.: The Dawros peridotite, Connemara, Eire, *Quarterly Journal of the Geological Society of London*, **113**, (1957), 1–26.

Scherer, G.W.: Crystallization in pores, *Cement and Concrete Research*, **29**, (1999), 1347–1358.

Shimizu, H., and Okamoto, A.: The roles of fluid transport and surface reaction in reaction-induced fracturing, with implications for the development of mesh textures in serpentinites, *Contributions to Mineralogy and Petrology*, **171**, (2016), 73.

Streit, E.E., Kelemen, P.B., and Matter, J.M.: Natural Carbonation of Peridotite and Applications for Carbon Storage, *AGU Fall Meeting Abstracts*, **2009**, (2009), U23A-02.

Viti, C., and Mellini, M.: Mesh textures and bastites in the Elba retrograde serpentinites, *European Journal of Mineralogy*, **10**, (1998), 1341–1359.